Simultaneous fluid and solid density measurements in swelling clay using X-ray microtomography and 3D particle tracking

Fabien Bernachy-Barbe, Kevin Alvarado

Simultaneous fluid and solid density measurements in swelling clay using X-ray microtomography and 3D particle tracking

Fabien Bernachy-Barbe*[a], Kevin Alvarado[a]

[a]Université Paris-Saclay, CEA, Service d'Etude du Comportement des Radionucléides, 91191, Gif-sur-Yvette, France

*Corresponding author:

fabien.bernachy-barbe@cea.fr, Tel: (+33)1 69 08 28 61, ORCID ID: 0000-0001-6432-5427

Abstract

In order to demonstrate the safety of engineered barriers for radwaste geological repositories, rich characterizations of bentonite hydro-mechanical behaviour are essential. X-ray Computed Tomography was used as the single input to measure both the full displacement field and water content in a heterogeneous bentonite sample resaturated in quasi-isochoric conditions. Since large texture changes do not allow the use of Digital Volume Correlation, this was achieved using 3D particle tracking to provide the kinematics in combination with calibrated and beam hardening-corrected grey levels. Matching the grey level sampling with those of kinematics using a mesh-based analysis, results show the development of heterogeneous swelling inside the cell and a final solid density gradient in the direction of water flow.

Keywords

Bentonite, particle tracking, full-field measurements, X-ray Computed Tomography

Article

1.   Introduction

Understanding the hydromechanical behaviour of bentonite swelling clays is an essential aspect of the safety demonstration for the plugs and seals of planned geological repositories for intermediate and high-level radioactive waste [1–3]. Indeed, these engineered barriers ensure the proper closure of repositories with a material showing low water permeability, efficient retention of radionuclides, and the development of a swelling pressure allowing closure of gaps in the barrier and cracks in the host rock created during the excavation process. The reaching of a water saturated state of homogeneous mechanical and hydraulic properties however remains an important point, which requires models to extrapolate from experimental works at the laboratory scale up to the repository scale. Although homogenization is commonly observed in small laboratory experiments, with final states weakly dependent on the initial fabric (powder, pellets, blocks…), the development of heterogeneities upon saturation is also observed [4,5]. These lab-scale heterogeneities mostly take the form of density gradients in the direction of water flow. Final states of *in-situ* experiments may show indeed some large heterogeneities [6,7] that make reliable modelling of the mass transport mechanisms and the effect of heterogeneities on the performance of the barrier all the more necessary.

X-ray Computed Tomography (X-CT) [8], as a straightforward 3D imaging tool, has shown some use in imaging the mass redistribution process in bentonite upon resaturation, starting with [9], and recently with work such as [10–13]. This technique can provide quantitative results on the solid density evolution, in volume, but also on the water transport [14], through a combination of the grey levels from X-ray tomography (X-ray absorption) and kinematics from Digital Volume Correlation (DVC) [15,16]. This provides a general method for decoupling the effect of solid and liquid densities on the measured grey levels of tomographic images. However, for studying heterogeneous bentonite samples, DVC can be of little or no use considering the large textural changes on transformed images. Moreover, the material itself evolves from an initially granular behaviour (in the case of powder, pelletized material, or mixture), where the displacement is not necessarily continuous.

In the present work, simultaneous measurements of the clay mass redistribution and water transport was achieved for a macroscopically heterogeneous sample making use of a 3D particle-tracking approach, such as used frequently for granular materials and powder sciences [17,18] in X-ray tomography. Upon water resaturation, large changes in the material fabric required the addition of dense markers in the bentonite, whose displacement was measured instead of the bentonite powder grains themselves. The method was illustrated on a powder sample presenting heterogeneities such as technological voids (incomplete filling) and segregation of fine powder. Due to the large heterogeneities relatively to the voxel size (pixels can initially correspond to powder grains or voids) and the initially discontinuous displacement field, a mesh-based averaging procedure was used. The kinematics, in combination with X-ray absorption from the tomography, allowed simultaneous 3D measurements of the solid and liquid density in these averaging elements.

2. Experimental methods and analysis

2.1 Resaturation and image acquisition

A simple *in-situ* hydration apparatus was designed for the purposes of hydrating centimetre scale bentonite samples in quasi-isochoric conditions (Figure 1). It is composed of a PEEK (PolyEtherEtherKetone) cell 6.5 mm thick with an attached force sensor (HBM U10M-25kN) in contact with the sample through a ball joint. The hydration is performed at near zero pressure through the bottom piston and a porous PE (PolyEthylene) plate. The air is allowed to escape the sample through a similar setup at the top, the system being only leak tight to low-pressure water. The system can accommodate samples 57 mm in diameter, of variable heights, with a precisely adjustable preload using a fine adjustment screw at the top, locked in position after at the beginning of the test. The bottom part of the system is designed to be repeatably positioned on the X-CT sample holder to submillimetre/subdegree accuracy although high-precision repositioning is not absolutely necessary to the procedure.

The method is illustrated here with a resaturation test performed on a powder sample of MX80 bentonite composed of crushed pellets, containing therefore a fine granular fraction. This powder was conditioned at a mass water content of 5.8%. As a marker, and reference

82   absorption material, zirconia (ZrO_2) is selected since it is X-ray opaque, chemically inert,
83   mechanically stiff and readily available in the form of small beads. Marker particles must
84   introduce minimal changes in the studied sample and follow the surrounding material. A small
85   amount (subgram) of 0.1 mm diameter ZrO_2 beads was added to the powder and mixed
86   thoroughly. This mix was poured directly into the testing apparatus then manually compacted.
87   Upon closure of the system, a preload of approximately 300 N was applied, a CT scan of the
88   initial state was carried out and then the hydration started. The sample parameters are
89   presented in Table 1.

90
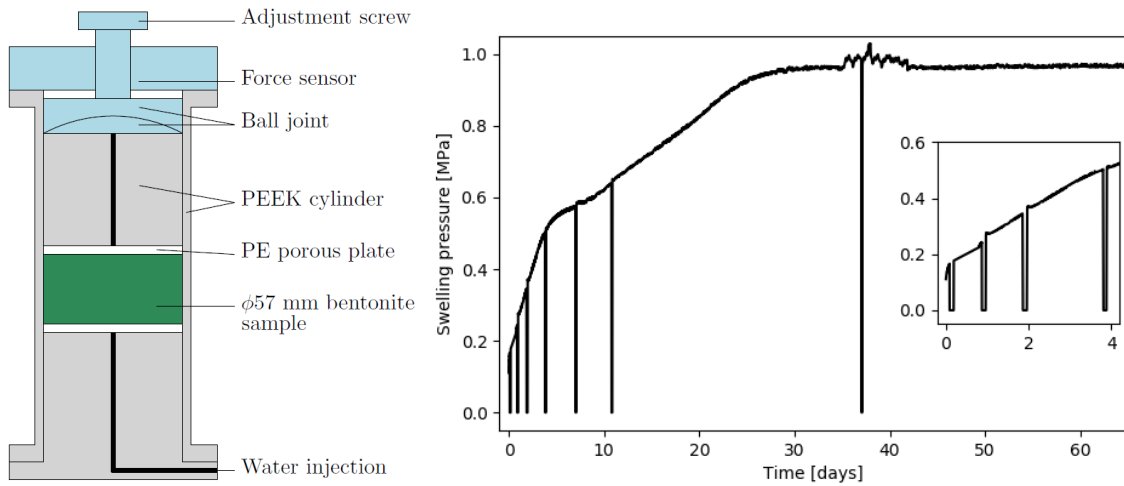
91
92   *Figure 1 : Schematic of the resaturation cell and graph of the swelling pressure development*
93   *as measured axially as a function of time. Signal interruptions correspond to X-CT scans.*

94

95   X-ray Computed Tomography was performed using a GE Phoenix v/tome/x m 240/180 CT
96   device using a directional X-ray tube. Acquisitions were carried out at variable intervals on the
97   swelling pressure curve by disconnecting the water injection line and moving the whole
98   apparatus in the CT enclosure. Water was always present in the injection area, that is not
99   emptied before scans. Eight scans from the initial state to saturation were carried out. These
100   acquisitions were performed in helical tomography mode [19] to minimize artefacts in general
101   at interfaces between materials, in particular in the horizontal plane corresponding to the
102   water injection surface. Acquisition parameters are detailed in Table 1; scan times are kept
103   approximately at 90 minutes to minimize the impact on the resaturation process. The volumes
104   of approximately 10 GB (16 bit grey levels) were reconstructed using GE proprietary
105   algorithms associated with the instrument, using in particular a manually tuned approximate
106   beam hardening correction. A refinement to this correction is described in the following parts.

107

108   Preliminary observations of the initial and final states (Figure 2) show reasonably artefact-free
109   images with contrast between the different materials in the volume of study, in particular
110   between bentonite and single zirconia beads. These beads need to be distributed throughout
111   the volume to obtain adequately dense measurements of the displacement field in the
112   following steps. Visible "densification" of the sample (increasing grey levels) correspond to the

effect of pore volume being filled with water. Some volume change is observable in the vertical direction due to the moderate stiffness of the PE porous discs. The hydration history (Figure 1) shows classical swelling pressure development [3] with a final value of 0.96 MPa.

Mass (g)	100.0	Tube voltage (kV)	210
Water content	5.8%	Tube current (µA)	150
Dry mass (g)	94.6	Detector pixel size (µm)	200 (binning 2×2)
Diameter (mm)	57	Image size (pixel)	$2000^2 \times 1362$
Initial height (mm)	27.1	Resolution (µm)	37.0
Dry density (g/cm^3)	1.365	Integration time (ms)	3×333
Initial porosity (cm^3)	35.3	Filtering	0.5 mm Sn

Table 1: Initial properties of the sample and acquisition parameters.
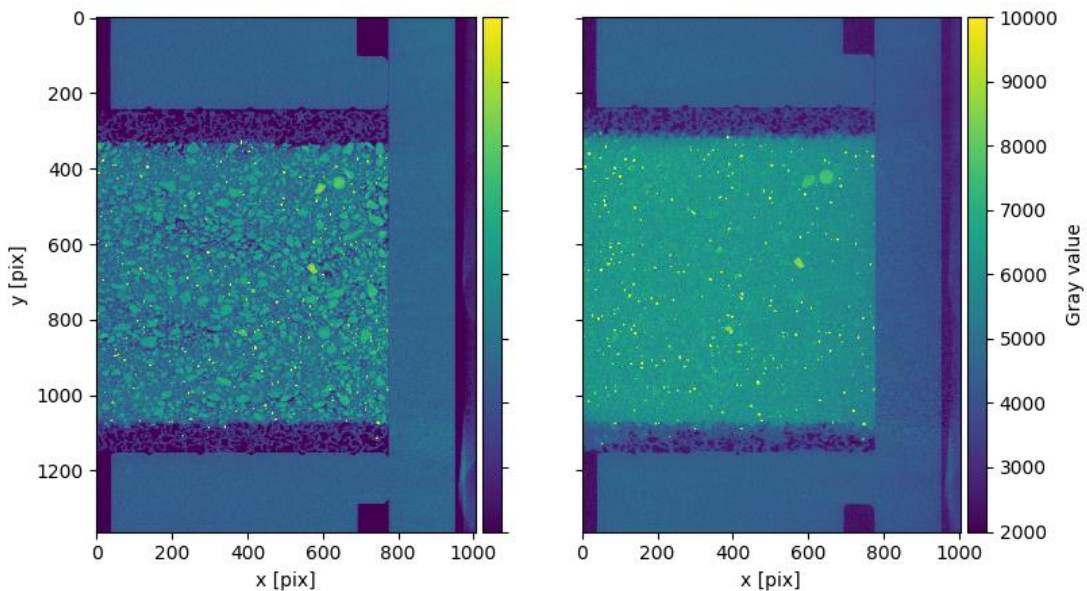
Figure 2 : Vertical X-ray tomography slices (half) of the initial state and saturated state in the apparatus.

2.2 Particle tracking and displacement measurements

Particle tracking was carried out using the Python package trackpy [20] (free software). Its tools allow multidimensional particle finding, tracking and analysis with parallel computation capabilities for large volumes of data. It uses the Crocker-Grier algorithm [21] that is essentially split into a particle identification algorithm (finding markers in all images), coordinate refinement algorithm (measuring accurately marker positions with subpixel accuracy) and a linking algorithm (labelling markers between frames). The particle positions and labels allow reconstructing particle trajectories in time.

The particle identification algorithm finds local maxima of a spatial bandpass-filtered image, with a characteristic size corresponding to an *a priori* known marker size (here 11 pixels). The

4

134   basic refinement algorithm [22] is initialized with the previously found positions and refines

135   positions by computing the local brightness-weighted centroid of the pixels around that

136   location. Let $[x, y, z]$ be the (initially integer) coordinates of a local maximum in grey level G

137   identified previously. Particles being assumed to be spherical of radius r, it is refined to sub-

138   pixel accuracy by iteratively updating the coordinates by the amount:

139
$$\begin{bmatrix} \Delta x \\ \Delta x \\ \Delta x \end{bmatrix} = \frac{1}{m} \sum_{i^2+j^2+k^2<r^2} \begin{bmatrix} i \\ j \\ k \end{bmatrix} G(x+i, y+j, z+k)$$

140

141   Here m is the integrated brightness over the sphere of radius r. A first quality filter is

142   introduced by bounding the so-called mass m of the markers to include sufficiently bright

143   features. Finally the linking step labels particles to identify them between frames. Requiring a

144   particle displacement to be sufficiently smaller than interparticle spacings, the software looks

145   for particles in the next frame within a certain search range. Since each particle can be

146   associated to several particles on the next frame, a solution is selected assuming Brownian

147   motion of particles, where the probability to find a particle exponentially decreases as a

148   function of distance. The optimal choice maximises the product of individual probabilities of

149   presence.

150

151   The final set of trajectories is then filtered: only uninterrupted trajectories (with markers

152   identified on all eight frames); and trajectories without displacement jumps (defined as

153   trajectories where one of the frame-to-frame distances is greater than four standard

154   deviations) are kept. In the present example, 16293 particles are fully tracked and used for

155   displacement measurements. In order to build a continuous displacement field from discrete

156   measurements, positions are averaged using markers contained in blocks of size (N×N×N)

157   pixels and an interpolation function is built using Radial Basis Function (RBF) interpolation

158   from the formed irregular grid ("multiquadric" type function $f(r) = \sqrt{1 + (r/N)^2}$). The scale

159   N=90 pixels (3.33 mm) is selected for the purpose of graphical representation herein.

160

161   Finally, the full Green-Lagrange strain fields are computed by numerical differentiation of the

162   RBF interpolated field. Its E_{zz} and E_{rz} components for three frames are presented in Figure 3

163   in θ-averaged maps. The frame 1 E_{zz}, 5 hours after the start of hydration shows a quite flat

164   swelling region on the bottom 5 mm of the sample, the rest of the sample being moderately

165   compacted by the swelling pressure of the bottom regions. Frame 3, 1 day and 20 hours after

166   the start, shows that half of the sample is swelling and the other half is more heavily

167   compacted. The extreme top of the sample, where some technological voids are present

168   (incomplete filling) are subject to the greatest level of axial compaction of order 15%. Shear

169   (E_{rz}) of order 5% at the cell walls show the occurrence of friction. The final state (frame 7)

170   shows a global swelling of the sample due to some deformation of the PE porous plates.

171   Interestingly, the bottom part of the sample where fast swelling previously happened remains

172   a large positive strain region; some moderate re-compaction of the first few millimetres is
173   however observable.

174
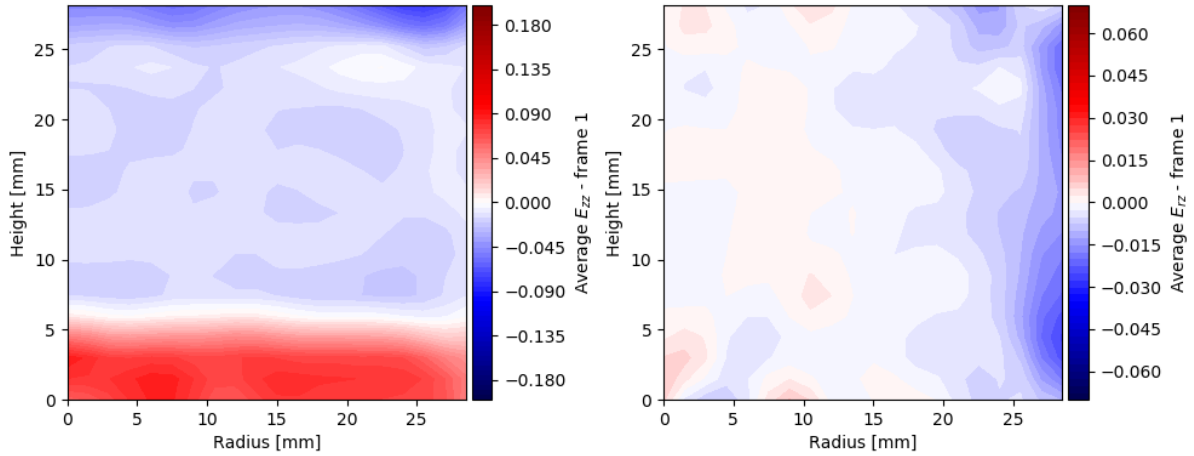
175

176
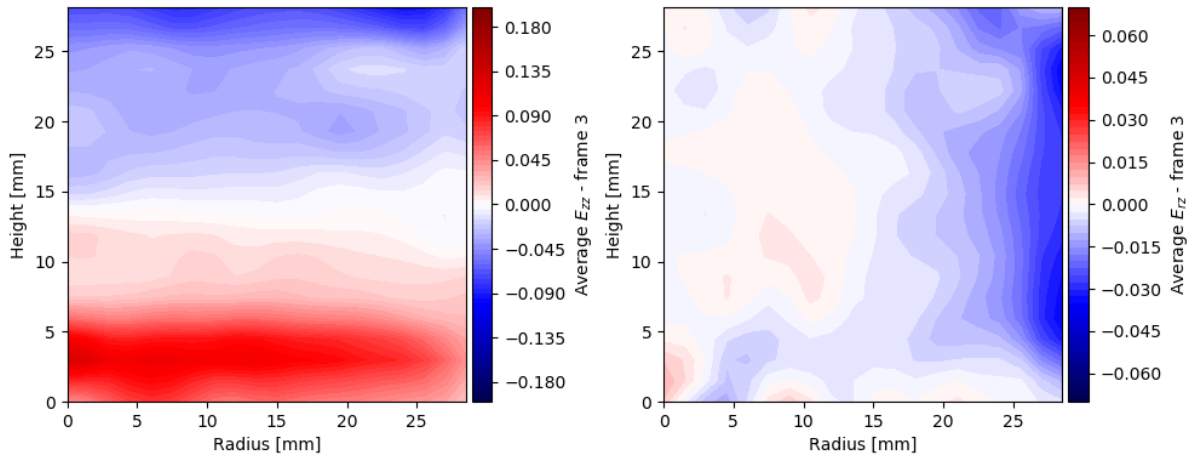
177   *Figure 3 : ϑ-averaged maps of the axial and shear components of the Green-Lagrange strain*
178   *tensor at frames 1, 3 and 7.*

179

180   **2.3   Marker-based artefact correction and grey level analysis**
181   Following the reasoning of [14], mass attenuation coefficients of solid (clay) and water can be
182   linearly combined to form the effective mass attenuation coefficient of the material :

183
$$\mu_t = \mu_s \rho_s + \mu_w \rho_w$$

184

In practice, the grey levels are observed to be in an affine relationship with the underlying partial densities of solid and water:

$$G = C + \alpha_s \rho_s + \alpha_w \rho_w \qquad (1)$$

Where C is an offset constant mostly dependant on hardware and reconstruction parameters. "Opacities" α_s and α_w are also observed to be dependent on instrumental variables and must also be experimentally determined. The two-step calibration procedure uses constant regions of the images to obtain comparable grey levels between frames. First, air and PEEK regions (on artefact free, rotation axis areas) and the ZrO_2 markers average grey level are used to calibrate frames one relative to another. In the second step, the grey level of pure water (observable in four frames) and the average grey level of the initial state (where both dry density and water content are known) are used to uniquely determine the α_s, α_w and C parameters for all frames.

Images are however subject to beam hardening (BH) artefacts that are incompletely corrected (or over-corrected) by the proprietary reconstruction software used. It may introduce large errors when performing density measurements. Moreover the water diffusion may induce time-dependant artefacts. The images can be self-corrected for BH by considering the requirement that marker brightness must be homogeneous (in a statistical sense) and must not exhibit large scale spatial dependencies, such as [23]. The true G value is the measured G_m up to some artefact field f_{BH} (of average 1 on the whole volume of interest to avoid calibration issues):

$$G_m = G \times f_{BH}(r, \theta, z)$$

The sample and the testing apparatus are approximately cylindrically symmetric. Neglecting the other components, one postulates a simple form for the radial component that fits the shape of the artefact and of average 1 over the whole sample, that is:

$$G_m = G \times (1 + A(r^2 - \frac{Q^2}{2}) + B(r^4 - \frac{Q^4}{3}))$$

With Q the sample radius. The A and B parameters are fitted by minimizing the spread of the average values of the marker brightness per radial bin. The number of bins in the radial direction is selected at 7 in order to capture only large scale variations. The effect of this correction is shown in the radial distribution of marker brightness in Figure 4 where frame 0 has some moderate residual BH and frame 7 strong overcorrection. The corrected images shown no large-scale radial dependency of the particle-integrated brightness. The initial density of the sample at placing was estimated at 1.365 in average. However, as observable in Figure 2, pixel grey levels are extremely variable due to the high resolution used (pixel size 37.0 µm versus powder grain size up to approximately 3 mm). Pixels may be located at markers, air voids, powder grains or in regions with unresolvable fine grains. Such fine description of the heterogeneity (powder grain scale) is beyond the scope of the current work since it is much smaller than the sampling of the displacement field obtained at marker

225 locations. In order to combine kinematic information from particle tracking with the local grey
226 values, compatible spatial sampling of the fields must be reached.
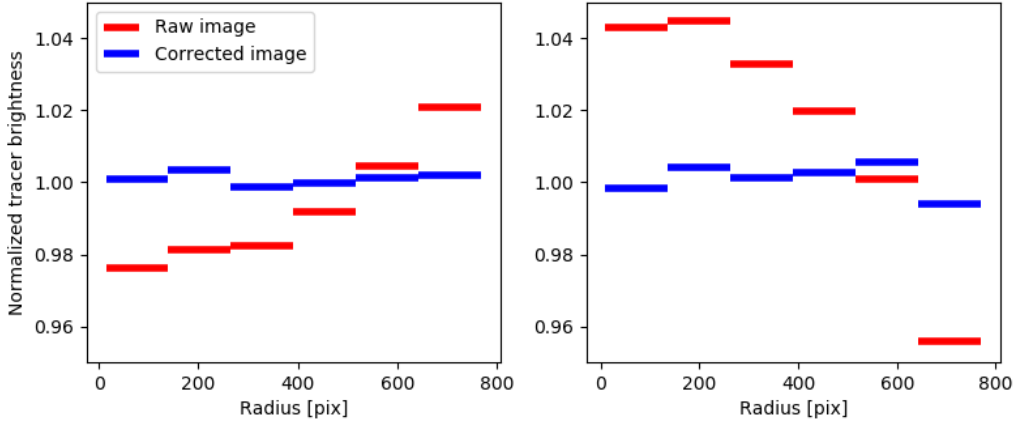
227
228 *Figure 4 : Normalized radial distribution of marker integrated brightness before and after BH*
229 *correction for frame 0 (left) and frame 7 (right).*
230

2.4 Density fields

232 Since the displacement field is sampled at random locations but the X-ray absorption is
233 sampled finely on an orthogonal grid, areas with a coarse description of the kinematics must
234 be matched with an adapted (coarser) image resolution. It is indeed required that volume
235 change measurements be performed on a region where the average change in grey level is
236 measured. This procedure is based on a triangulation of the images: a tetrahedral mesh is built
237 using marker locations as points for 3D Delaunay triangulation. The image is then
238 "triangulated" where the average grey level per tetrahedron in all images is computed.
239 Deformed meshes for each image are directly obtained from the updated marker positions of
240 the particle-tracking algorithm. One can therefore compute in an elementary way the local
241 volume change by computing the volume change of each tetrahedron, which can be
242 compared, assuming element-wise approximate mass conservation, to the average grey level
243 evolution. Combining equation 1 with the mass continuity equation leads to the following
244 system expressing the increment of the solid and water partial densities as a function of the
245 local volume change and the grey level increment:

246
$$\begin{cases} \Delta\rho_s = -\rho_{0s}\left(\dfrac{V_0}{V} - 1\right) \\ \Delta\rho_w = \dfrac{\Delta G - \alpha_s\Delta\rho_s}{\alpha_w} \end{cases}$$

247
248 with V_0/V the ratio of initial and final tetrahedron volumes, ΔG the corresponding local grey
249 level variation on the corrected, triangulated image. The full analysis workflow is summarized
250 in Figure 5. Some final filtering of the density fields can be performed at the post-processing
251 stage based on the quality of tetrahedral elements, reasonable values of the element volumes
252 and element volumetric deformations.
253

254
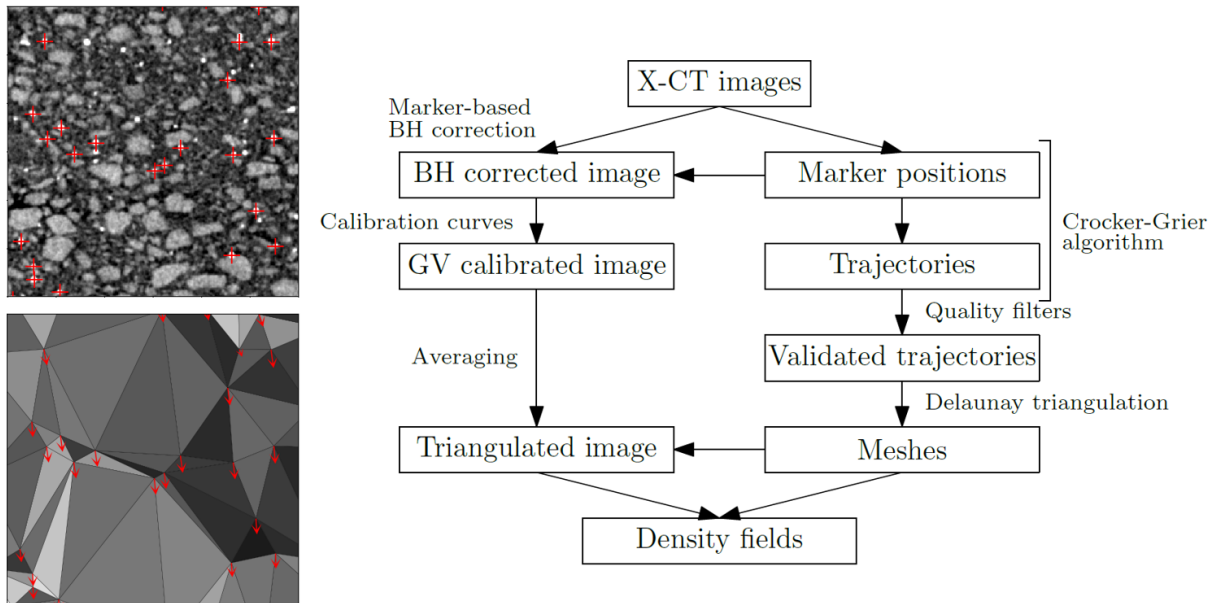
Figure 5 : Simplified schematic of the algorithm. The top left image represents a 2D example of initial data with markers located; bottom left image represents the final triangulated image with displacement vectors at nodes.

Figure 6 shows an example of processing for in θ-averaged maps for frame 3. The importance of the BH correction on the density fields is observed on the top part of the figure: the differences in BH between frames are much larger than the true grey level variations due to density changes. The kinematics are summarized on the middle-left image showing the value of the volumetric strain where positive values indicate swelling (decrease in solid density) and negative values compaction. In particular, as seen on the initial solid density (middle-right) the initially low density regions at the top of the sample characteristic of incomplete filling coincide with regions of negative volume change, as they are compacted (homogenized) throughout the swelling process. Final results on the bottom show the water content field with an almost saturated bottom region, a transition area and a top part with the initial water content. The solid density evidences the development of a gradient in the direction of flow caused by the differential swelling of bottom and top parts of the sample.

This entire scenario is summarized in the vertical profiles of water content and solid density on Figure 7. The initial water content and the average dry density match exactly the experimental value since they are used for calibration purposes. Post-mortem measurements on the sample were carried out to measure the water content (water loss at 105°C for 24 hours) and dry density (hydrostatic weighing in oil). The calculated profiles can therefore be compared to validate the method. Water content is in good correspondence with the measured values (40.2% versus 40.7% directly measured); dry density is also reasonably measured (1.315 versus 1.301 directly measured) taking into account that sample extraction may artificially underestimate density due to swelling and damage. The water content evolution is characteristic of 1D hydration. The dry density evolution confirms the scenario

proposed previously [5] where differential swelling of top and bottom parts of the sample as well as changes in stiffness create "non-monotonous" mass fluxes; this results in a final dry density gradient at saturation.
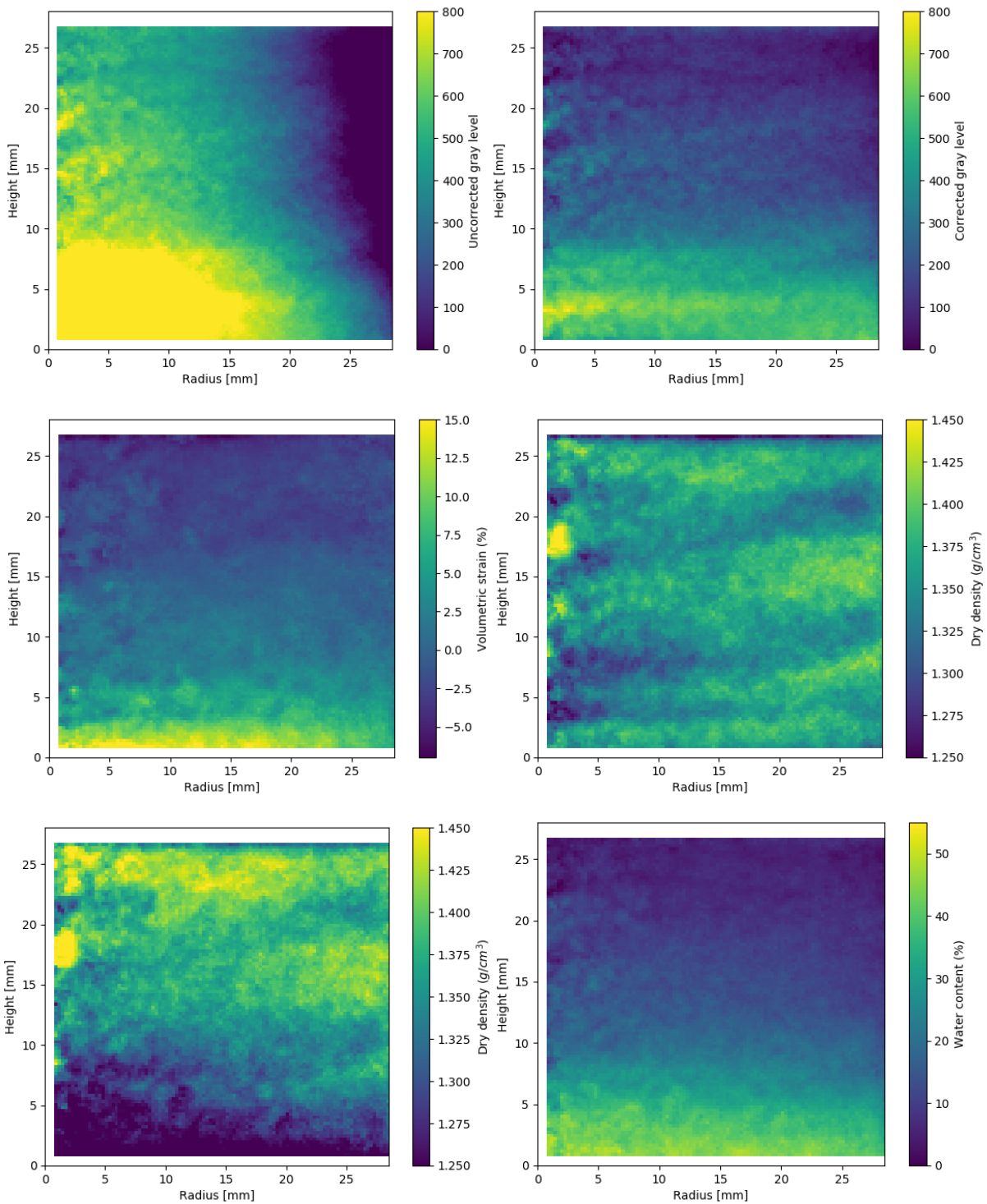
Figure 6 : Example of processing for ϑ-averaged maps of frame 3 (transient state). Top row: uncorrected and beam-hardening corrected difference images between frame 3 and frame 0; middle row: volumetric strain from mesh elements and initial dry density; bottom row: current solid density and water content.

The material is largely homogenized at the small scale. However, comparing the initial and final heterogeneities of the sample, it can be observed that the hydration process has resulted in an overall increase of the large scale heterogeneity. The standard deviations of the dry density field are 0.11 g/cm^3 initially and 0.14 g/cm^3 at saturation. This increase in heterogeneity is largely due to the final density gradient.
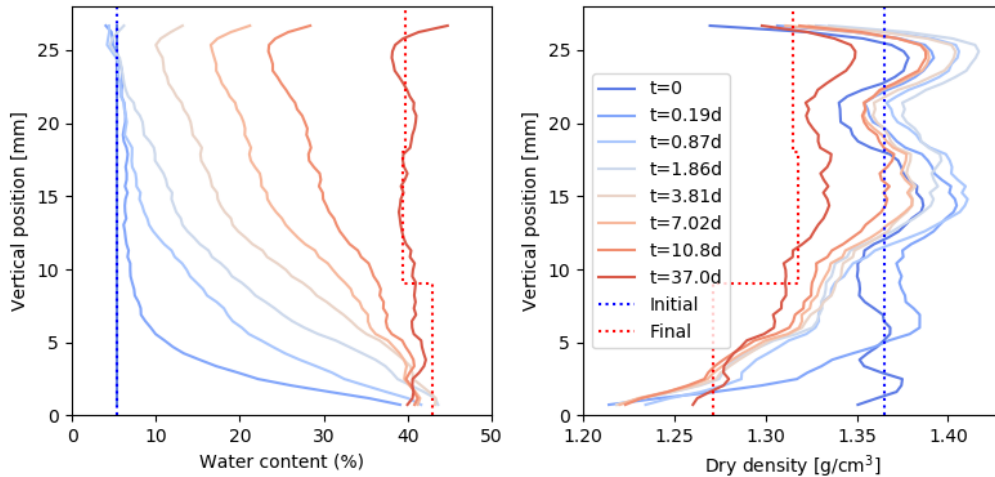
Figure 7 : Final water content and dry density vertical profiles as a function of time compared with the known initial and final states.

3.   Conclusions

3D X-CT particle tracking was applied successfully in bentonite to obtain kinematic information in order to derive full-field water and clay densities evolutions as a function of time. The method was presented on a simple case with moderate heterogeneity (swelling of a powder sample with approximate cylindrical symmetry. Only density heterogeneities at a scale comparable with the local refinement of the description of the kinematics were considered using a tetrahedron-wise averaging procedure. It was shown that careful calibration of images and correction of the beam-hardening artefact (using the apparatus and particle themselves) was required to obtain accurate results. Combining grey level evolutions and the measured displacement fields, evolutions of water content and dry density fields confirmed a known scenario of bentonite resaturation at constant volume. If small-scale (grain size) heterogeneity seems to be reduced upon resaturation, a large-scale solid density gradient in the direction of flow was clearly observed. The occurrence of friction at cell walls was also observed indirectly through as the shear strain component. Future work will aim at applying this methodology to general heterogeneous samples, and use full-field information to calibrate and validate numerical models of bentonite hydro-mechanical behaviour.

References

[1] R. Pusch, 11 - Development and application of smectitic buffer and backfill materials in geological repository systems, in: Geol. Repos. Syst. Safe Dispos. Spent Nucl. Fuels Radioact. Waste, Woodhead Publishing, 2010: pp. 323–352. https://doi.org/10.1533/9781845699789.3.323.

[2] P. Delage, Y.J. Cui, A.M. Tang, Clays in radioactive waste disposal, J. Rock Mech. Geotech. Eng. 2 (2010) 111–123. https://doi.org/10.3724/SP.J.1235.2010.00111.

[3] Y.-J. Cui, On the hydro-mechanical behaviour of MX80 bentonite-based materials, J. Rock Mech. Geotech. Eng. 9 (2017) 565–574. https://doi.org/10.1016/j.jrmge.2016.09.003.

[4] WP4 deliverable, Bentonite mechanical evolution (BEACON) project D.4.1 – experimental work for the support of model development and validation, 2019.

[5] F. Bernachy-Barbe, N. Conil, W. Guillot, J. Talandier, Observed heterogeneities after hydration of MX-80 bentonite under pellet/powder form, Appl. Clay Sci. 189 (2020) 105542. https://doi.org/10.1016/j.clay.2020.105542.

[6] J.C. Mayor, M. Velasco, Long-term Performance of Engineered Barrier Systems (PEBS) project D.2.1-8 - EB dismantling synthesis report, 2014.

[7] C. Svemar, L.-E. Johannesson, P. Grahm, D. Svensson, O. Kristensson, M. Lönnqvist, U. Nilsson, Prototype Repository – Opening and retrieval of outer section of Prototype Repository at Äspö Hard Rock Laboratory – Summary report, SKB AB, 2016.

[8] E. Maire, P.J. Withers, Quantitative X-ray tomography, Int. Mater. Rev. 59 (2014) 1–43. https://doi.org/10.1179/1743280413Y.0000000023.

[9] M. Van Geet, G. Volckaert, S. Roels, The use of microfocus X-ray computed tomography in characterising the hydration of a clay pellet/powder mixture, Appl. Clay Sci. 29 (2005) 73–87. https://doi.org/10.1016/j.clay.2004.12.007.

[10] S. Saba, J.-D. Barnichon, Y.-J. Cui, A.M. Tang, P. Delage, Microstructure and anisotropic swelling behaviour of compacted bentonite/sand mixture, J. Rock Mech. Geotech. Eng. 6 (2014) 126–132. https://doi.org/10.1016/j.jrmge.2014.01.006.

[11] L. Massat, O. Cuisinier, I. Bihannic, F. Claret, M. Pelletier, F. Masrouri, S. Gaboreau, Swelling pressure development and inter-aggregate porosity evolution upon hydration of a compacted swelling clay, Appl. Clay Sci. 124 (2016) 197–210. https://doi.org/10.1016/j.clay.2016.01.002.

[12] A. Molinero Guerra, N. Mokni, P. Delage, Y.-J. Cui, A.M. Tang, P. Aimedieu, F. Bernier, M. Bornert, In-depth characterisation of a mixture composed of powder/pellets MX80 bentonite, Appl. Clay Sci. 135 (2017) 538–546. https://doi.org/10.1016/j.clay.2016.10.030.

[13] A. Molinero Guerra, Y.-J. Cui, N. Mokni, P. Delage, M. Bornert, P. Aimedieu, A.M. Tang, F. Bernier, Investigation of the hydro-mechanical behaviour of a pellet/powder MX80 bentonite mixture using an infiltration column, Eng. Geol. 243 (2018) 18–25. https://doi.org/10.1016/j.enggeo.2018.06.006.

[14] T. Harjupatana, J. Alaraudanjoki, M. Kataja, X-ray tomographic method for measuring three-dimensional deformation and water content distribution in swelling clays, Appl. Clay Sci. 114 (2015) 386–394. https://doi.org/10.1016/j.clay.2015.06.016.

[15] B.K. Bay, T.S. Smith, D.P. Fyhrie, M. Saad, Digital volume correlation: Three-dimensional strain mapping using X-ray tomography, Exp. Mech. 39 (1999) 217–226. https://doi.org/10.1007/BF02323555.

[16] M.A. Michael A., J.-J. Orteu, H.W. Schreier, Volumetric Digital Image Correlation (VDIC), in: H. Schreier, J.-J. Orteu, M.A. Sutton (Eds.), Image Correl. Shape Motion

370   Deform. Meas. Basic ConceptsTheory Appl., Springer US, Boston, MA, 2009: pp. 1–16.
371   https://doi.org/10.1007/978-0-387-78747-3_8.

372 [17] D.M. Mueth, G.F. Debregeas, G.S. Karczmar, P.J. Eng, S.R. Nagel, H.M. Jaeger,
373   Signatures of granular microstructure in dense shear flows, Nature. 406 (2000) 385–389.
374   https://doi.org/10.1038/35019032.

375 [18] S.A. McDonald, L.C.R. Schneider, A.C.F. Cocks, P.J. Withers, Particle movement during
376   the deep penetration of a granular material studied by X-ray microtomography, Scr.
377   Mater. 54 (2006) 191–196. https://doi.org/10.1016/j.scriptamat.2005.09.042.

378 [19] H.E. Martz, C.M. Logan, D.J. Schneberk, P.J. Shull, X-Ray imaging: Fundamentals,
379   industrial techniques and applications, CRC Press, 2016.
380   https://doi.org/10.1201/9781315375199.

381 [20] D. Allan, C. van der Wel, N. Keim, T.A. Caswell, D. Wieker, R. Verweij, C. Reid, Thierry,
382   L. Grueter, K. Ramos, apiszcz, zoeith, R.W. Perry, F. Boulogne, P. Sinha, pfigliozzi, N.
383   Bruot, L. Uieda, J. Katins, H. Mary, A. Ahmadia, soft-matter/trackpy: Trackpy v0.4.2,
384   Zenodo, 2019. https://doi.org/10.5281/zenodo.3492186.

385 [21] J.C. Crocker, D.G. Grier, Methods of Digital Video Microscopy for Colloidal Studies, J.
386   Colloid Interface Sci. 179 (1996) 298–310. https://doi.org/10.1006/jcis.1996.0217.

387 [22] C. van der Wel, D.J. Kraft, Automated tracking of colloidal clusters with sub-pixel
388   accuracy and precision, J. Phys. Condens. Matter. 29 (2016) 044001.
389   https://doi.org/10.1088/1361-648X/29/4/044001.

390 [23] T. Oesch, F. Weise, D. Meinel, C. Gollwitzer, Quantitative In-situ Analysis of Water
391   Transport in Concrete Completed Using X-ray Computed Tomography, Transp. Porous
392   Media. 127 (2019) 371–389. https://doi.org/10.1007/s11242-018-1197-9.

393